energies

MDPI

Article

First Look at Safety and Performance Evaluation of Commercial Sodium-Ion Batteries

Rachel Carter [1,*], Gordon H. Waller [1], Connor Jacob [2], Dillon Hayman [2], Patrick J. West [3] and Corey T. Love [1]

[1] Chemistry Division, US Naval Research Laboratory, Washington, DC 20375, USA
[2] Excet, Inc., A Precise Systems Company, Springfield, VA 22150, USA
[3] ASEE/NRL Postdoctoral Associate, Washington, DC 20375, USA
* Correspondence: rachel.c.ashmore.civ@us.navy.mil

Abstract: Herein, we investigate the performance and safety of four of the early-stage, commercial Na-ion batteries available in 2024, representing the most popular cathode types across research and commercialization: polyanion (Na-VPF), layered metal oxide (Na-NMF), and a Prussian blue analog (Na-tmCN). The cells deliver a wide range of energy density with Na-tmCN delivering the least (23 Wh/kg) and Na-NMF delivering the most (127 Wh/kg). The Na-VPF cell was in between (47 Wg/kg). Capacity retention under specified cycling conditions and with periodic 0 V excursions was the most robust for the Na-tmCN cells in both cases. Accelerating rate calorimetry (ARC) and nail penetration testing finds that Na-NMF cells do undergo thermal runaway in response to abuse, while the Na-VPF and Na-tmCN exhibit only low self-heating rates (<1 °C/min). During these safety tests, all cells exhibited off-gassing, so we conducted in-line FTIR equipped with a heated gas cell to detect CO, CO_2, CH_4, toxic acid gases (HCN, HF, NH_3), and typical electrolyte components (carbonate ester solvents). Gases similar to those detected during Li-ion failures were found in addition to HCN for the Na-tmCN cell. Our work compares different types of commercial Na-ion batteries for the first time, allowing for a more holistic comparison of the safety and performance tradeoffs for different Na-ion cathode types emerging in 2024.

Keywords: sodium-ion battery; accelerated rate calorimetry; safety testing; commercial cells

check for updates

Academic Editor: Carlos M. Costa

Received: 20 December 2024
Revised: 3 January 2025
Accepted: 5 January 2025
Published: 31 January 2025

Citation: Carter, R.; Waller, G.H.; Jacob, C.; Hayman, D.; West, P.J.; Love, C.T.. First Look at Safety and Performance Evaluation of Commercial Sodium-Ion Batteries. *Energies* **2025**, *18*, 661. https://doi.org/10.3390/en18030661

Copyright: © 2025 by the authors. Licensee MDPI, Basel, Switzerland. This article is an open access article distributed under the terms and conditions of the Creative Commons Attribution (CC BY) license (https://creativecommons.org/licenses/by/4.0/).

1. Introduction

Sodium-ion (Na-ion) batteries were first demonstrated alongside Li-ion batteries with Whittingham's demonstration of intercalation into TiS_2 in 1978 [1] and Doeff's full cell in 1993 [2]. However, Na's lower energy density and inability to intercalate into a graphite anode contributed to limited research emphasis and commercialization of the chemistry. More recently, beginning in the 2010s, key components of the Li-ion battery supply chain, like cobalt and lithium, became strained, resulting in the Li-ion battery demand outpacing production and supply [3]. Since that time, Na-ion battery research and commercialization has regained momentum [4–6]. In the early 2020s, companies like CAT'L (China) and Faradion (UK, India) began producing large quantities of cells (>10 GWh) with energy densities comparable to lithium iron phosphate (LFP) Li-ion batteries (~150 Wh/kg).

With resurging interest in Na-ion batteries, research grade cells and material analysis began indicating attractive features of Na-ion batteries, which address weaknesses of the ubiquitous Li-ion battery [5,7]. These include long cycle life [8], high rate capability [9–11], stability during 0 V storage [12], and a higher degree of safety [13,14]. However, features like cycle life and safety are difficult to assess prior to scaleup, as demonstrated during the

maturation of Li-ion batteries [15,16]. Performance and safety are both strongly influenced by parameters like electrolyte quantity, electrode thickness, and form factor. From a performance perspective, electrolyte quantity impacts lithium inventory, while the thickness and form factor impact impedance and rate capability [17]. From a safety perspective, the electrolyte quantity influences cell volatility and total capacity, and the form factor influences failure mode severity.

High-energy-density batteries like Li-ion batteries exhibit thermal runway, which is a cascade of chemical reactions initiated by the short circuit-induced heating of volatile electrolyte solvents and culminating with cathode combustion [18,19]. The careful diagnosis of thermal runaway in Li-ion batteries revealed that onset is correlated to the quantity and volatility of electrolyte and severity to cathode composition [19]. Cathode composition is the primary variable among commercial Li-ion batteries with layered metal oxides like NMC (nickel, manganese, cobalt oxide) and olivine structures like LFP (lithium iron phosphate) being the most popular. However, cathode composition is more widely varied in 2024 commercial Na-ion batteries [20].

Due in part to Na's distinct compatibility with other cell materials compared to Li, the wide range of materials in commercial Na-ion batteries to date makes the assessment of performance and safety difficult [10]. The most common anode material is hard carbons, since Na cannot intercalate into graphite like Li. Na is stored at defect sites and pores of the hard carbons, achieving similar capacities to Li in graphite but requiring an additional sodiation step to mitigate additional SEI growth [21]. Recently, research is accelerating on higher energy density alloy and intercalation anodes [10]. Electrolytes tend to contain similar components to Li-ion: -PF_6 or -TFSI-based salt, carbonate solvents, and small quantities of additives. Finally cathodes, which dictate the cell specific capacity, primarily fall into three main categories: layered metal oxides, polyanions, and Prussian blue analogs [6,10,22]. Briefly, the layered transition metal oxide cathodes ($Na_xM_1 \ldots M_nO_2$, n = number of metals, M = Ni, Fe, Mn, Cu, Ti, Co, etc.) [20] deliver the highest capacity and are the most like NMC Li-ion cathodes, exhibiting layered structures and propensity for catastrophic thermal runaway. Na polyanion cathodes are similar to the olivine LFP with an open framework to facilitate high rates and high structural and thermal stability providing less severe failure modes. The initial research attempted simply replacing the Li in LFP ($NaFePO_4$); however, the compound was unstable, leading to the incorporation of components like V and PO_2, which present toxicity and cost concerns. Finally, Prussian blue analogs (PBAs, $NaM_1[M_2(CN)_6]$ M_1 = Ni, Cu, Zn, Mn, etc. M_2 = Fe) boast low cost and an open channel framework, which is promising for high rates. These materials were not compatible with the smaller Li cation, but they have gained popularity with Na-ion batteries as well as larger ions like potassium (K). PBAs are challenged by complicated synthesis and water instability. Safety insights are not yet available.

As well documented in the Li-ion battery literature, the cathode type is a key factor in the cycle life and rate capability and dictates thermal runway severity when comparing cells with similar anodes and overall construction, motivating similar comparative research on Na-ion batteries. Despite the larger size (atomic and ionic) compared to Li^+ ions, Na^+ ions undergo faster solid-state diffusion in Na-ion cathodes, which may be due to the closer size matching of the cation and the interatomic spacing of the host [23], resulting in high rate capability (>50C) [4]. Further, the thermal stability of Na-ion cathodes suggests higher temperatures to initiate their combustion and lower relative oxygen content to fuel the combustion [24]. However, recent publications presenting early demonstrations of Na-ion battery performance and safety explore only one cathode type at a time with limited tests [9,12–14,25–31]. Thermal runaway is typically induced by external heating to assess safety. The most quantitative of the heating techniques is heat–wait–seek (HWS) using

accelerating rate calorimetry (ARC) tests, which heat in small increments, allowing the accurate detection of onset of self-heating temperatures and approximating adiabaticity to allow the calculation of chemical energy released during failure [18]. Physical abuse tests like nail penetration allow for an analysis of response to packaging failures or accidents. Finally, off-gas analysis is important to understand the toxicity of gases released during venting or thermal runaway. Gas chromatography-mass spectroscopy (GC-MS) or Fourier transform infrared spectroscopy (FTIR) are the most common gas analysis techniques [32–34] and are often employed on collected samples, which can result in an under-detection of reactive or condensed species. This work explores the performance (energy, power, and 0 V storage stability) and safety (ARC, nail penetration and time resolved FTIR off-gas analysis) of four commercial Na-ion batteries with cathodes from each of the three main categories (polyanion, layered metal oxide, and Prussian blue analog), allowing for assessment of the strengths and weaknesses of each type for the first time.

2. Methods and Materials

Commercial Na-ion batteries from four vendors and Li-ion batteries from two vendors were obtained and cycled galvanostatically using a Maccor, Tulsa, OK, USA battery cycler and Maccor, Tulsa, OK, USA thermal chamber according to specifications provided by the cell manufacturers. Skin temperatures were tracked with 18-gauge T-type thermocouples secured around the cell midpoint with electrical tape. Zero-volt tests were conducted by discharging the cells to 0 V, below the manufacturer specified lower cutoff voltage for all cells (Table 1), on the Maccor and resting for 5 h followed by conventional cycles to probe performance recovery. A Thermal Hazard Technology (THT) EV ARC was utilized for accelerating rate calorimetry (ARC) heat–wait–seek (HWS) measurements, thermal ramp experiments, and nail penetration. The HWS procedure involves heating in small increments, waiting for the system to equilibrate, and then seeking to see if the sample is heating faster than the chamber at a rate >0.02 °C/min. When self-heating is detected, the chamber approximates an adiabatic environment heating at the same rate as the sample until a safety temperature of 300 °C is reached [18]. During thermal ramps of ~1.6 °C/min, a Thermo Scientific Norristown, PA, USA in line Antaris IGS Gas Analyzer, RESULTS, Omnic, and Flow version 2.0 was used to collect off-gas analysis via a 180 °C heated line attached to a sealed pressure vessel and purged with N_2 gas. The closed system ensured the off gases were detected and the heated line prevented them from condensing before detection. Fluoropolymer gas sampling lines were used to minimize the loss of highly reactive acid gases, including HF. The reference spectra for gases of interest at varied concentrations were utilized for gas concentration measurements, which is assessed in specific regions with minimized interference with other gases (Figure S4). THT pneumatic nail penetration actuated with 1500 psi N_2 gas was used as an additional abuse method to characterize external damage to the cells.

Table 1. Properties and nomenclature of each Na-ion battery tested.

Label	Voltage Range (V)	Nominal Capacity (Ah)	Cathode Type
Na-VPF	2–4.25	0.7	$Na_vV_x(PO_4)_yF_z$
Na-NMF1	1.5–4.1	1.5	$Na(Ni_xFe_yMn_z)O_2$
Na-NMF2	1.8–3.95	1.3	$Na(Ni_xFe_yMn_z)O_2$
Na-tmCN	1.00–1.81	4.3	$Na_xtm[Fe(CN)_6]$

3. Results and Discussion

The performance of four commercial Na-ion cell types with different cathodes (Table 1) was first assessed with galvanostatic cycling at a symmetric C/2 rate, which was within

the specification for each cell. The second cycle is plotted in Figure 1A. The polyanion cathode (Na-VPF) exhibited the highest voltage reactions at ~3.5 and ~4.1 V but the lowest fraction of its reported nominal capacity (~76.8%) at a C/2 rate. The high-voltage nature of the reaction was previously reported for similar $Na_vV_x(PO_4)_yF_z$ cathodes [8,9,12]. The layered metal oxide cells (Na-NMF1 and Na-NMF2) have the next highest voltage reactions at ~3.75 V and ~2.5 V, consistent with other $Na(Ni_xFe_yMn_z)O_2$ reports [11,14,25], and delivered 89.4% and 96.4% of their respective nominal capacities. Finally, the Prussian blue analog cathode (Na-tmCN) exhibits the lowest voltage reaction at ~1.5 V but delivers 104.8% of its nominal capacity. The Na-tmCN cathodes utilize specific transition metals (tm) inside the $Na_xtm[Fe(CN)_6]$ unit cells at each electrode to control the reaction voltage and electrode stability [22]. Simply comparing the voltage responses to a C/2 cycle emphasizes the wide range of behaviors possible in the Na-ion battery category as a result of different active materials and charge storage mechanisms.

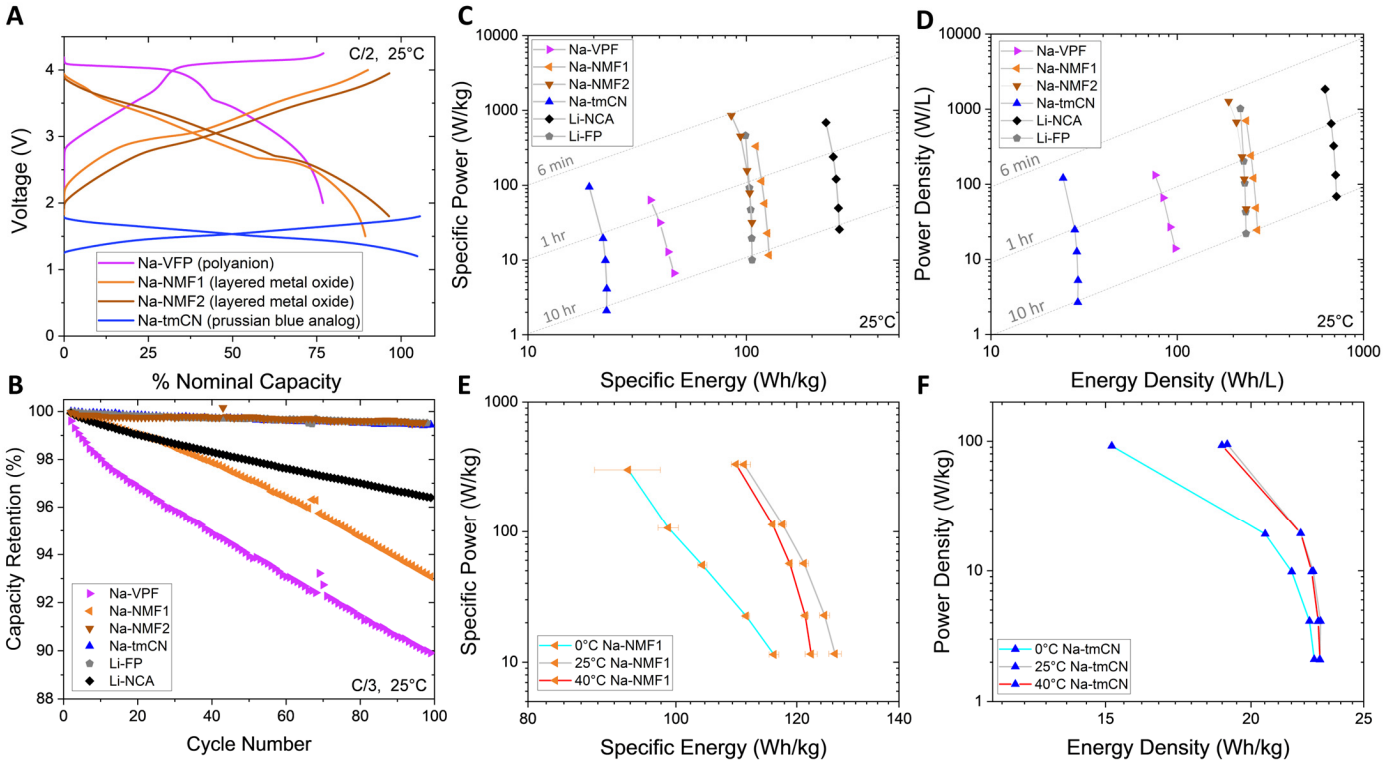

Figure 1. (**A**) Galvanostatic charge/discharge curves for each Na-ion battery distinguished by the cathode active material type, (**B**) capacity retention over 100 cycles, mass (**C**) and volume (**D**) specific Ragone plots up to 3C discharge rate for each Na-ion battery and an NCA and LFP based Li-ion battery, mass specific Ragone plot of Na-NMF (**E**) and Na-tmCN (**F**) at 0, 25, and 40 °C.

The cycling stability of these cells was then assessed with CC-CV charging at a C/3 rates and compared to commercial Li-ion batteries with the two most popular cathode types (NMC and LFP). The Li-FP, Na-NMF2, and Na-tmCN cells deliver high capacity retention (>99% capacity retention after 100 cycles). The higher resolution of the capacity retention during the cycling of these cells is provided in Figure S1. In contrast, the Na-VPF and Na-NMF1 cells experience more rapid capacity loss than Li-NMC cells, and the Na-VPF cell experience the most severe decay (~0.1% capacity/cycle). One of the more surprising observations of cycle life retention is the very different capacity retention behaviors for the two cells with similar cathode chemistries, Na-NMF1 and Na-NMF2. These differences are likely linked to the varied quality of manufacturing and cell details like electrolyte selection. Overall, these findings do not confirm the overall assertion that Na-ion batteries exhibit a

longer cycle life than Li-ion, since (1) the quality of Na-ion commercial cells varies and is not yet be equivalent to state-of-the-art Li-ion and (2) different active materials will likely present different capacity retentions, and only three types were tested.

Within the specification sheet parameters (voltage ranges and peak currents), the power and energy density of each Na cell is compared to the same Li cells (Li-NMC and Li-FP) on Ragone plots normalized to cell mass and volume (Figure 1C,D). The Na-tmCN and Na-VPF cells exhibit lower energy density than Li-ion cells, and the Na-NMF1 and Na-NMF2 cells exhibit similar performance to Li-FP. The Na-NMF1 cells deliver slightly higher energy density while the Na-NMF2 cells deliver slightly higher power density. The Na-tmCN cell was not tested at its highest rate due to the current limits of our cyclers, but overall, the Na cells did not exhibit power densities exceeding the Li cells. Finally, the Na-NMF1 and Na-tmCN cells were tested at 0 °C and 40 °C. At 40 °C, the Na-NMF1 cell achieved close to the nominal energy density regardless of the applied current: delivering 127 Wh/kg and 122 Wh/kg at C/5 and 3C, respectively. In contrast, lowering the temperature to 0 °C resulted in suppressed energy densities that were rate dependent with the Na-NMF1 delivering 109 Wh/kg at C/5 and 93 Wh/kg at 3C. The Na-tmCN cell was less impacted by temperature with slightly less energy density at the lowest temperature (0 °C) and the highest rate (5C), 15.2 Wh/kg vs. 18.8 Wh/kg, and no difference in performance at 40 °C compared to 25 °C.

Along with the rate testing, surface-mounted type-T thermocouples were used to detect heat generation during cycling. During a 1C discharge (Figure 2A), the skin temperature for each cell (Figure 2B) in a fan-cooled chamber set to 25 °C was assessed. In agreement with other observations, the cells reached their highest temperature at the end of discharge [35]. The peak temperatures of the Na-ion batteries were lower than those of the Li-ion batteries. This is likely a result of the differing specific heat and their overall lower energy densities, which are visualized in Figure 2C. Interestingly, while the Na-NMF1 and NA-NMF2 discharge profiles are similar, the Na-NMF2 cell exhibits a higher temperature rise. This suggests that both electrode chemistry and cell engineering influence cell heating. At 1C, heat generation is largely composed of resistive heating that can be influenced by cell level factors like the applied current, thickness of the electrodes, and tab placement. Further assessment is required, but these initial observations indicate that less thermal management may be required for Na-ion batteries compared to Li-ion batteries.

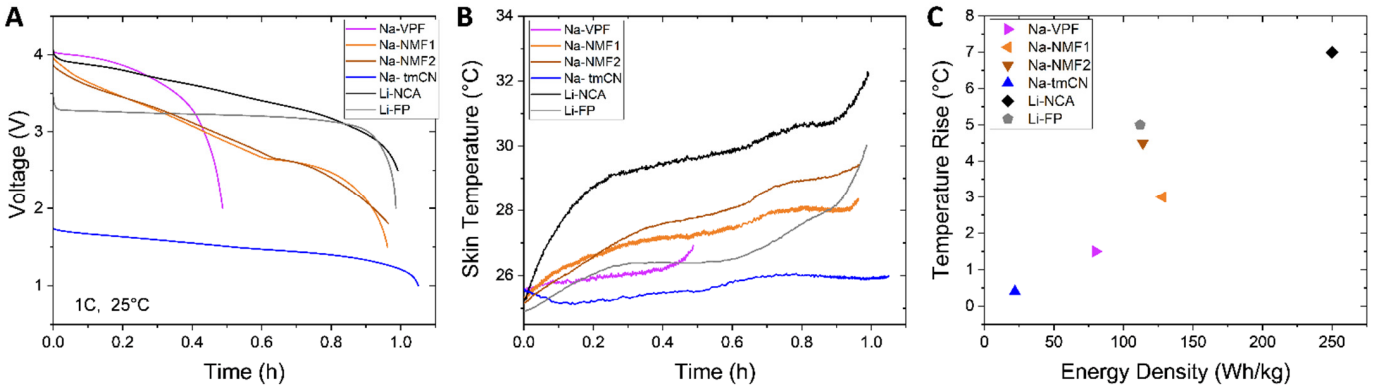

Figure 2. (**A**) Voltage profiles during 1C discharge. (**B**) Skin temperature of various cells during 1C discharge. (**C**) Peak temperature rise after 1C discharge plotted with respect to cell energy density.

We went on to test the resilience of the Na cells to 0 V excursions, since Na-ion batteries can effectively utilize aluminum (Al) for both current collectors. Li-ion batteries must employ copper (Cu) as an anode current collector to prevent Li alloying with Al at low voltages. Therefore, if Li-ion batteries are discharged below 0.5 V, as the cathode voltage falls, the

anode voltage rises enough for Cu to oxidized to Cu^{+} or further to Cu^{2+}. These ions are released into the electrolyte, etching away the anode current collector and altering current flow. Then, in a subsequent charge, the ions can be redeposited as Cu^{0} metal, introducing a risk of internal short circuit [12,36,37]. This phenomenon is avoided by controlling the Li-ion discharge voltage typically to no less than 2.5 V and storing cells at states of charge (SOC) above 0%, typically 20–30%. However, since Na does not alloy with Al, their anodes can employ Al current collectors. Therefore, Na-ion batteries can be stored safely at 0 V and 0% SOC, providing a "deactivated" condition desirable for safe storage and transport [12,38].

In order to test the stability of the cells in the low-voltage range, the cells were discharged to 0 V after a normal C/2 charge and discharge and then rested for 5 h (Figure 3A). This process was repeated every 5th cycle and compared to Li-FP and Li-NCA cells (Figure 3B). The Li-NCA cell exhibited more rapid capacity loss than in its normal operating regime (0.036% compared to 0.12%, Figure 1B), which was presumably due to dissolution of the Cu current collector. The Li-FP cell did not exhibit this sort of capacity loss over these 6 excursions. Perhaps it has a higher N:P ratio than the Li-NCA cell, providing some built-in resilience to 0 V excursions. The Li-FP, Na-NMF1, NMF2, and Na-tmCN cells proved more resilient to over discharge than the Li-NCA cell. However, the Na-VPF cell rapidly decayed with 0 V excursions [12]. With Cu dissolution no longer a risk in Na cells, other undesirable behaviors like further SEI growth or transition metal dissolution from the cathode are more likely contributors to the decay of the Na-VPF cell. Figure 3C plots the capacity delivered below the cutoff voltage indicating the varying degree of additional electrochemical activity in that region. However, the cells passing greater capacity below their cutoff do not correlate to those decaying quicker under 0 V excursion. The Na-VPF, Na-NMF1, and NMF2 cells pass minimal capacity (<10% nominal), which is likely due to further SEI growth or capacitive charge storage. However, the Na-tmCN cell exhibits an additional plateau at ~0.5 V, indicating an additional reaction delivering another 37% of the nominal capacity, which proves reversible, since minimal to no capacity loss is observed with multiple 0 V excursions. While some Na-ion batteries are more robust to 0 V storage than others, these findings emphasize Na-ion batteries' unique capability for 0 V storage not accessible to Li-ion batteries.

The remainder of this work focuses on safety analysis, beginning with the accelerating rate calorimetry (ARC). Each Na-ion battery was fully charged (100% SOC) and tested using the heat–wait–seek (HWS) technique to accurately assess safety parameters like onset of self-heating and peak self-heating rates (Figure 4A). Among the Na-ion cells tested, only the Na-NMF1 and Na-NMF2 presented behavior consistent with Li-ion battery thermal runaway [15,18]. The Na-NMF1 cell began self-heating at 87 °C and then vented at 134 °C and spiked in temperature to 442 °C. The Na-NMF2 cell had a similar vent temperature to Na-NMF1 at 125 °C but did not exhibit self-heating until 147 °C followed by a peak temperature of 487 °C. The delayed self-heating could be due to a different electrolyte formulation or safety features provided in manufacturing. Despite the cell (Na-NMF2) going into thermal runaway, its later onset indicates a higher degree of safety. The Na-tmCN cell started in a similar manner to the Na-NMF2 cell with a vent at 96 °C followed by self-heating at 177 °C; however, no thermal runaway was detected in this cell. The Na-tmCN cell maintained mild self-heating rates (<1 °C/min) until the experimental cutoff temperature of 300 °C was reached. Finally, the Na-VPF cell exhibited self-heating at the lowest temperature, 51 °C, which was followed by a vent at 98 °C. Mild self-heating was maintained in the Na-VPF cell until ~200 °C, where the self-heating rate dropped below 0.02 °C/min and the system re-entered HWS mode. Self-heating was minimal beyond 200 °C until the experimental cutoff of 300 °C was reached.

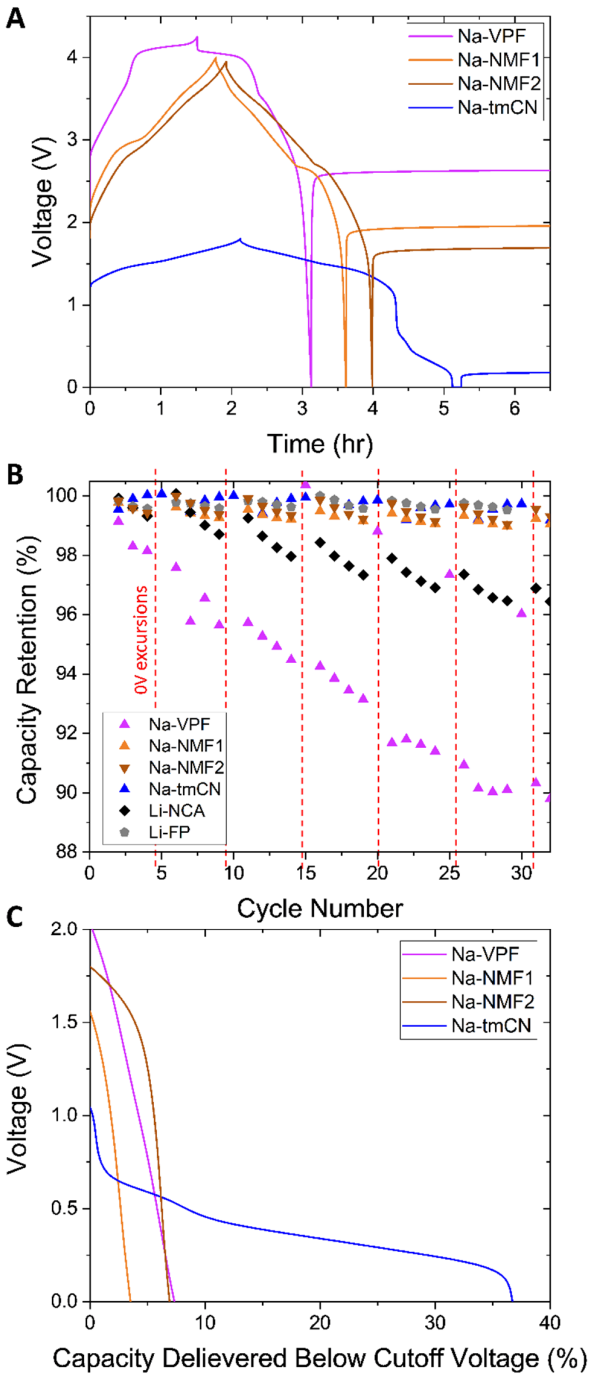

Figure 3. (**A**) C/2 galvanostatic charge and discharge followed by a 0 V excursion and 5 h rest, (**B**) % nominal capacity delivered below the normal cutoff voltage during 0 V excursion, and (**C**) capacity retention over 35 cycles with a 0 V excursion and 5 h rest every 5th cycle.

These results are more easily compared on a temperature rate vs. temperature plot (Figure 4B) which includes the Li-NCA and Li-FP cells. The Na-VPF and Na-tmCN cells did not surpass the ~5 °C/min threshold for thermal runaway [18]. However, the Na-NMF1 and Na-NMF2 cells well surpassed that, reaching 5607 °C/min and 2528 °C/min, respectively. These peak temperature rates are much higher values than that of the Li-FP cell (7.2 °C/min) despite remarkably similar electrochemical energy density (Figure 1C,D). We went on to test if the Na-NMF1 and Na-NMF2 cells' thermal runaway severity reduced at lower SOCs (50, 25 and 0%). For the Na-NMF2 cell, we observed steadily lower peak temperatures (337, 309, and 274; Figure S2A) and self-heating rates (90, 13, and 0.62 °C/min;

Figure S2B). However, only the 0% SOC Na-NMF cell drops below the 5 °C/min threshold, indicating no thermal runaway. This measurement demonstrates that the 0% SOC case is inert to abuse in cells capable of thermal runaway. Reducing the Na-NMF2 cell's capacity to 50% results in prevention of thermal runaway. The 100% SOC Na-NMF2 cell had a high self-heating onset of 147 °C; at 50% SOC, this was increased to 161 °C and the self-heating rate peaks at only 1.2 °C/min.

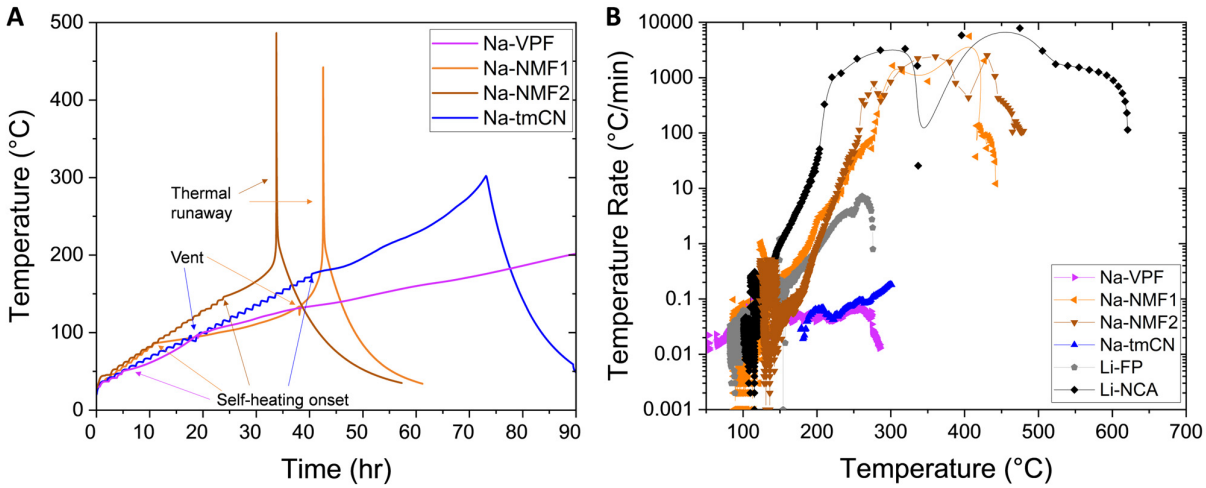

C

Cell Type	Onset Temp (°C)	Vent Temp (°C)	Peak Temp (°C)	Peak Temperature Rate (°C/min)
Li-NCA	87	112	620	7,867
Li-FP	90	153	276	7.2
Na-VPF	51	98	300*	0.14
Na- NMF1	87	134	442	5,607
Na- NMF2	147	125	487	2,528
Na-tmCN	177	96	300*	0.18

*300 °C is the calorimeter cutoff temperature.

Figure 4. (**A**) Accelerating rate calorimetry (ARC) heat–wait–seek (HWS) experiment for each Na-ion battery at 100% SOC, (**B**) temperature rate vs. temperature from (**A**) data with Li-NMC and Li-FP data incorporated. (**C**) Table summarizing important parameters from each cell tested.

In order to assess a failure mode not induced by heat, nail penetration was investigated (Figure 5). The reaction of the fully charged Na-ion cells to pneumatically actuated nail penetration revealed the resiliency of each cell to mechanical failure. The Na-VPF cell (Figure 5A) experienced slow voltage loss, self-heating to 114 °C, and minimal damage to the cell. In contrast, the Na-NMF1 cell rapidly lost voltage, reached a peak temperature of 409 °C, and was left with packaging damage, revealing the internal electrodes. The Na-NMF2 cell behaved much like the Na-VPF cell with slow voltage loss and self-heating to 132 °C, again indicating a higher degree of safety compared to the electrochemically similar Na-NMF1 cell. Finally, the Na-tmCN cell did not experience any self-heating upon nail puncture and maintained its cell voltage. In comparison to the Li-ion batteries (Figure S3), the severity of failure, based on peak self-heating rates, was Na-tmCN < Na-VPF < Na-NMF2 < Li-FP < Na-NMF1 < Li-NCA.

Since vent gases were apparent from each ARC and nail penetration test, we utilized an in-line FTIR-g setup to detect gases of interest, including combustion products (CO, CO_2, CH_4), toxic gases (HCN, HF, NH_3), and electrolyte carbonates (DMC, EMC, and PC). The cells were sealed in a pressure vessel and purged with N_2 before the thermal ramp experiments was completed to 180 °C. The concentration of gases detected is calculated by

comparing reference spectra at 180 °C and ranging ppm values in regions of the spectra that are not convoluted with other species of interest. The error between the experimental spectra and the reference spectra is plotted with the detected values throughout each experiment. Visualization of this process is provided in Figure S4A.

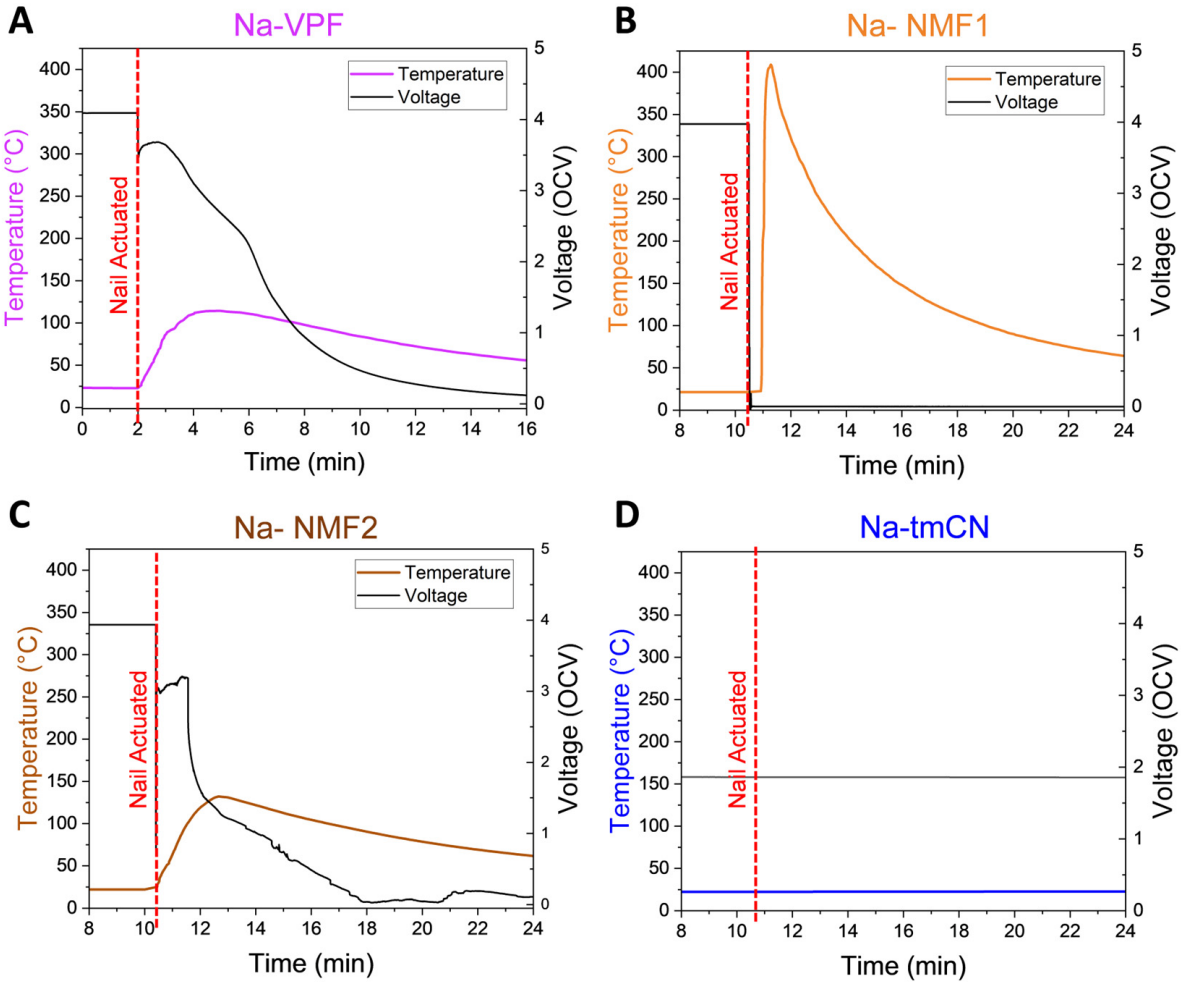

E

Cell Type	Peak Temp (°C)	Peak Temperature Rate (°C/min)	Mass Loss (%)	Physical Condition
Li-NCA	422	16,982	60.4	Rupture of packaging
Li-FP	214	630	17.5	Minimal damage
Na-VPF	114	274	6.1	Minimal damage
Na- NMF1	409	7,540	28.5	Rupture of packaging
Na- NMF2	132	287	2.0	Minimal damage
Na-tmCN	23	0.08	0	Maintaining voltage

Figure 5. Temperature (left y-axis) and voltage (black, right y-axis) responses to 1500 psi pneumatic nail penetration indicated by a red dashed line for each Na-ion battery (**A**–**D**). (**E**) Table summarizing important parameters from each cell tested.

Beginning with the Na-VPF cell (Figure 6A), we observed a spike in the temperature ramp at ~100 °C, which was in conjunction with the detection of several gases. CO, CO_2, and CH_4 were detected in the range of ~300–800 ppm, which was indicative of material combustion. HF was also detected at 25 ± 5 ppm (Figure 6B). Following the first detected gases, carbonates were detected as the electrolyte was boiled through the now open cell vents. PC was detected first peaking at ~150 ppm, followed by DMC up to 400 ppm, and

finally EMC up to 800 ppm. DMC and EMC present in order of their boiling points, 90 °C and 107 °C, respectively, but PC is observed well below its boiling point of 242 °C. As the test progressed, the cell was heated until 180 °C was reached, while CO, CO_2 and HF evolved a second time with less intensity around 175 °C.

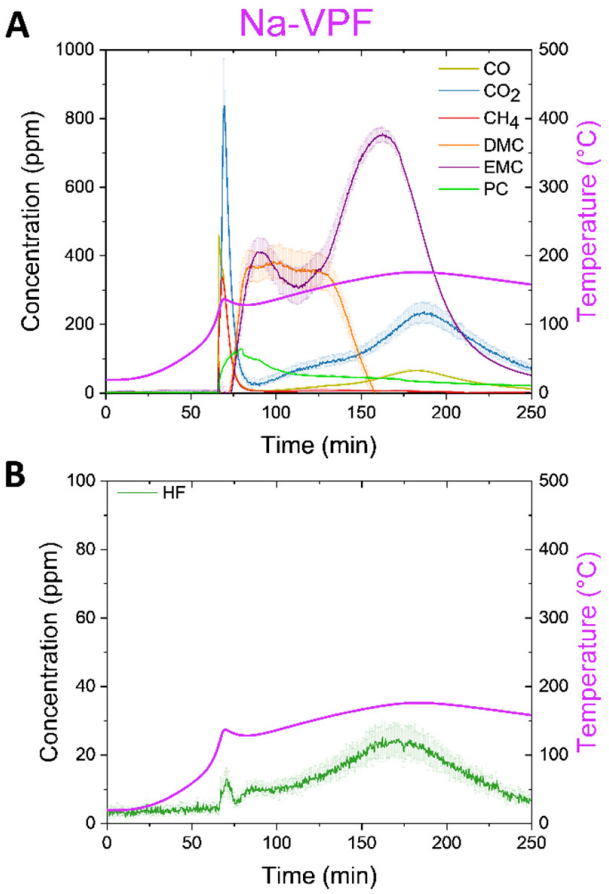

Figure 6. Thermal ramp of the Na-VPF cell charged to 100% SOC was carried out up to 180 °C to examine off gases. The cells were sealed in a pressure vessel purged with N_2 and connected with a heated line (180 °C) to an FTIR-g system. (**A**) The concentration of CO, CO_2, CH_4, and carbonates is plotted over the duration of the thermal ramp on the left y-axis and with error in the measurement a shaded region above and below the corresponding line. The skin temperature is plotted in magenta on the right y-axis. (**B**) The concentration of HF over the duration of the thermal ramp on the left y-axis again with the skin temperature on the right y-axis.

Next, the Na-NMF cells were investigated. First, the Na-NMF1 cell, which has evidence of both vent and thermal runaway along the orange temperature curve (Figure 7A), much like in the cell's ARC data (Figure 4A), was investigated. These features correlate with the detection of large concentrations of combustion gases (CO, CO_2 and CH_4) up to 10,000 ppm at the vent (~150 °C) and up to 50,000 ppm at the thermal runaway (~200 °C). Other gases were detected at smaller quantities (Figure 7B), as seen in Figure 6B. Notably, carbonates were detected up to 500 ppm prior to the cell venting at ~100 °C. They are detected in a similar order and quantity to the Na-VPF cell: first PC, then DMC, and finally EMC. The similarities between these detected gases in the Na-VPF and Na-NMF1 cells indicate that the electrolytes are likely similar. However, the detection of the carbonates prior to venting in the Na-NMF1 cell presents concern about the quality of cell manufacturing, allowing leaking and delaying venting. At thermal runaway, HF is detected at 14 ± 8 ppm (Figure 7C). Due to the relatively high degree of error, HF detection was compared to the reference spectra in

Figure S4A, confirming peaks in the proper range for the Na-VPF, Na-NMF1, and Li cells. In stark difference to the Na-NMF1 cell, the Na-NMF2 cell does not experience thermal runaway during the thermal ramp experiments; just a vent is detected at ~140 °C (Figure 7D), which is a finding that was replicated twice (Figure S5). The lack of thermal runaway in thermal ramp experiments is due to the low self-heating rate of the Na-NMF2 cell below 200 °C (Figure 4B). At the cutoff temp of the thermal ramp (180 °C), the self-heating rate is ~0.26 °C/min well below the 5 °C/min threshold for thermal runaway. The Na-NMF2 cell did experience thermal runaway during ARC testing (Figure 4A) but at a higher onset temperature than the Na-NMF1 cell (147 °C compared to 87 °C). The gases detected upon vent of the Na-NMF2 cell are first combustion gases CO and CO_2, followed by carbonates, much like the observations from the Na-VPF cell in Figure 5. In this cell, less PC and DMC were detected in exchange for more EMC, indicating a different electrolyte blend than the Na-VPF and Na-NMF1 cells. Carbonates were not detected prior to venting in the Na-NMF2 cell, in contrast to the Na-NMF1 cell; this indicates more robust sealing and vent mechanisms, which may explain its stability to higher temperature and the lack of thermal runaway in this test. Furthermore, HF was not detected (Figure 7E). This finding points to improved manufacturing, as the property provides a higher degree of safety in ARC, nail penetration, and thermal ramp tests, since the cell's active materials and electrochemical energy density are similar.

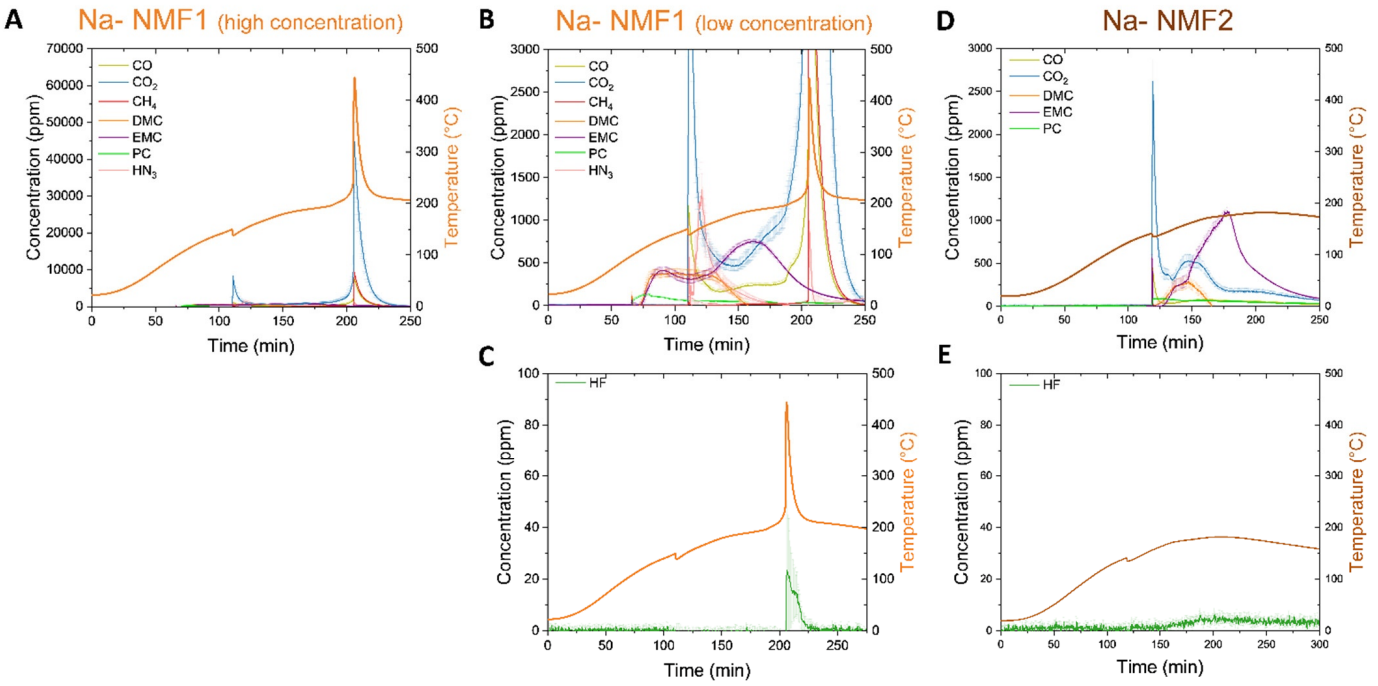

Figure 7. Thermal ramp of the Na-NFM1 and Na-NMF2 cells charged to 100% SOC was carried out up to 180 °C to examine off gases. The cells were sealed in a pressure vessel purged with N_2 and connected with a heated line (180 °C) to an FTIR-g system. (**A**) The concentration of CO, CO_2, CH_4, NH_3 and carbonates is plotted over the duration of the thermal ramp of Na-NMF1 on the left y-axis and with error in the measurement a shaded region above and below the corresponding line. The skin temperature is plotted in orange on the right y-axis. (**B**) A lower concentration regime of the same data in (**A**), revealing trends among the electrolyte components upon venting. (**C**) The concentration of HF over the duration of the Na-NMF1 thermal ramp on the left y-axis again with the skin temperature again on the right y-axis. (**D**) The concentration of CO, CO_2, CH_4, and carbonates is plotted over the duration of the thermal ramp of Na-NMF2 on the left y-axis and with error in the measurement a shaded region above and below the corresponding line. The skin temperature is plotted in burnt on the right y-axis. (**E**) The concentration of HF over the duration of the Na-NMF2 thermal ramp on the left y-axis again with the skin temperature again on the right y-axis.

Finally, the Na-tmCN cell was tested (Figure 5C). This cell was not sealed in a pressure vessel, making gas analysis less reliable. This cell shows one distinct feature in the temperature ramp, where the cell vented at ~120 °C, correlating with the peak detection of HCN gas to ~1400 ppm, which was followed by steady detection at ~500 ppm until the test was terminated (Figure 8A). With such a high detection of HCN, we again compared the instantaneous FTIR spectra to the reference spectra and confirmed agreement with peak shape and location (Figure S4B). After the cell breaching, CO was detected to about 80 ppm (Figure 8B) when the cell was heated to ~170 °C. Finally, ~20 ppm of NH_3 was detected near the end of the test at ~180 °C. Notably, like the Na-NMF1 cell, all three gases detected for the Na-tmCN cell were detected prior to cell venting beginning at around only ~50 °C. After the vent at ~86 min until ~160 min, the HN_3 detection was reported with >100% error. Investigating the FTIR spectra in this region revealed that HN_3 was not detected here. Therefore, this portion of the data was removed. In the region of high error, it is likely that a different gas that we did not fit the spectra for, which has some peaks in the fitted region of HN_3, was present. This emphasizes that we have not detected all gases formed in all experiments, especially hydrogen. However, we feel confident in the combustion products, carbonates, and acid gases that we are reporting for each cell.

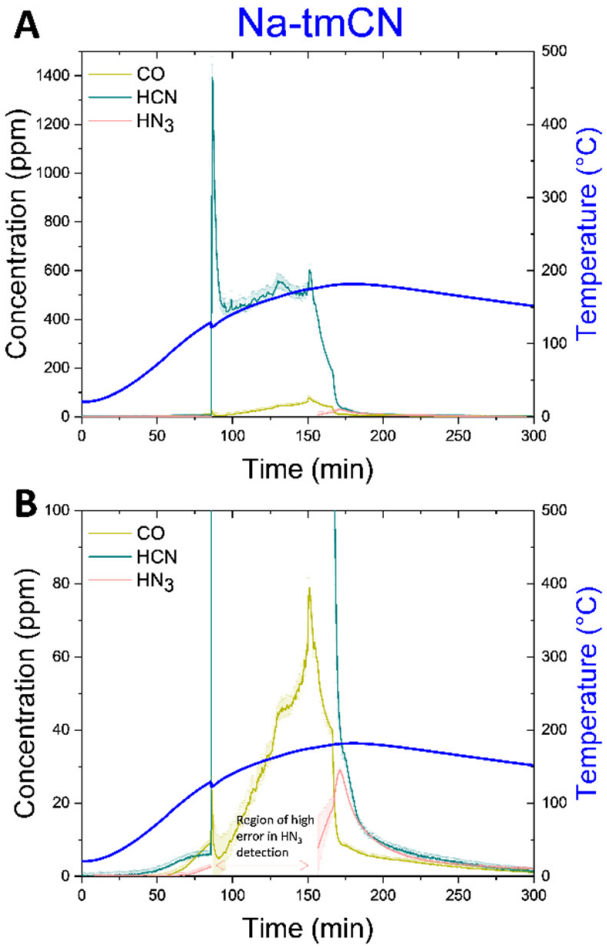

Figure 8. Thermal ramp of the Na-tmCN cells charged to 100% SOC was carried out up to 180 °C to examine off gases. The cells were placed in the ARC chamber, purged with N_2, and connected with a heated line (180 °C) to an FTIR-g system. (**A**) The concentration of CO, HCN, and NH_3 is plotted over the duration of the thermal ramp of on the left y-axis and with error in the measurement a shaded region above and below the corresponding line. The skin temperature is plotted in blue on the right y-axis. (**B**) A lower concentration regime of the same data in (**A**), revealing delayed increase in CO and NH_3 detection.

For fair comparison of the gases detected from each Na cell (Figures 6–8) and Li cell (Figures S6 and S7), the concentration in ppm is first converted to flow rate in mg/m^3 using Equation (1) and the ideal gas assumption that 1 mole of gas occupies 22.4 L.

$$V = c \times \frac{M}{22.4} \times \frac{273}{273 + T} \times \frac{P}{1013} \quad (1)$$

where V is the flow rate in g/m^3, c is the concentration in ppm, M is the molar mass of the gas, and T and P are the pressure inside the gas cell in Kelvin and mbar, respectively. The flow rate is then multiplied by the mass flow through the gas cell in (m^3/s) and the increments of time between measurements, 20 s, and summed over the duration of the test to obtain a mass. The mass of each detected gas was then normalized to cell energy in Wh in Figure 9. We note that for the Na-NMF, the concentrations of combustion gases are similar to Li-NMC, while for the Na-VPF and Na-NMF, the concentrations are similar to Li-LFP. Among the toxic gases analyzed, the most HCN is detected from the Na-tmCN cell, which contains CN in its unit cells. Similar concentrations (~10 ppm/Ah) of HF were detected from the Li-NMC, Li-FP, Na-VPF and Na-NMF cells. Finally, carbonates of similar concentrations were detected from the Li-NMC, Li-FP, Na-VPF and Na-NMF cells.

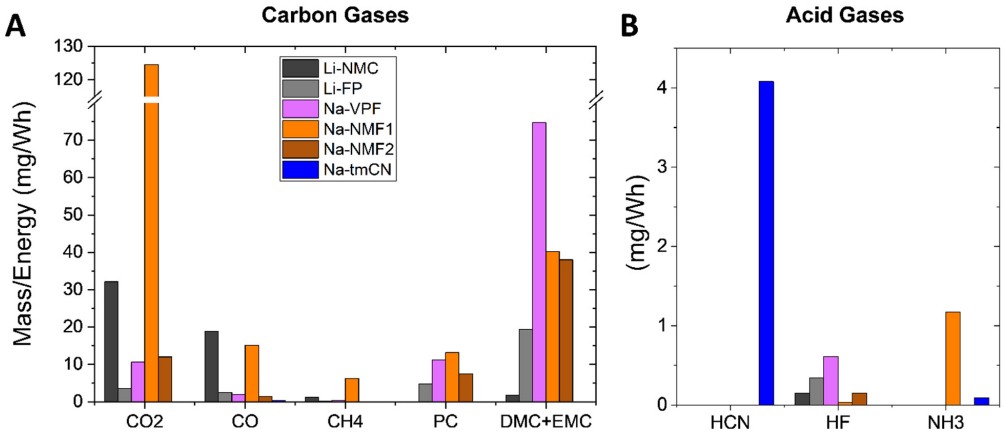

Figure 9. Total mass of each gas detected over the duration of the thermal ramp via FTIR-g of each Na-ion battery and a Li-NMC and Li-FP cell normalized by cell Wh. (**A**) is carbon-containing gases and the (**B**) is acid gases.

4. Conclusions

In conclusion, this work investigates three different commercial Na-ion batteries representing the cells containing the three most popular cathode types among research and commercialization (polyanion, transition metal oxide, and Prussian blue analogs). The Na-VPF, Na-NMF, and Na-tmCN deliver a wide range of energy density and safety behaviors emphasizing the diversity of the Na-ion battery market and the early stages of maturation of the commercially available cells. Some cell specific conclusions include the following: the Na-VPF cell exhibits poor cyclability but good safety response to thermal and physical insult; the Na-NMF cell delivers energy and power density comparable to Li-FP cells but has a lower degree of safety, and the Na-tmCN cell is robust to conventional and 0 V cycling and exhibits a high degree of safety but delivers a low energy density. We present a radar plot to emphasis parameters prominent in Na-ion batteries not provided by Li-ion batteries (rate capability, safety, and long cycle life) to emphasize the benefit of diversifying the battery landscape with this emerging chemistry. Finally, we want to emphasize that these are only four cells from four vendors, and the findings should be used for early assessment but not to generalize about each cathode type.

Supplementary Materials: The following supporting information can be downloaded at https://www.mdpi.com/article/10.3390/en18030661/s1, Lower SOC ARC tests for Na-NMF1 and Na-NMF2 cells. Li-ion thermal ramp and nail penetration tests. HF, HCN, and HN_3 detections compared to FTIR-g standards. Figure S1: Capacity retention over cycle as shown in Figure 1B over a 1% decay region to show the differences between Na-NMF2, Na-tmCN, and Li-FP; Figure S2: (A) Accelerating rate calorimetry (ARC) heat-wait-seek (HWS) experiment for Na-NMF1 cells at 0%, 25%, 50%, and 100% SOC, (B) temperature rate vs. temperature from (A) data with Li-FP at 100% SOC data incorporated, showing that only the 0% SOC Na-NMF1 cell exhibits a more benign failure than the 100% SOC Li-FP cell. (C) Accelerating rate calorimetry (ARC) heat-wait-seek (HWS) experiment for Na-NMF2 cells at 50%, and 100% SOC, (D) temperature rate vs. temperature from (C) data with Li-FP at 100% SOC data incorporated, showing that reducing the SOC of the Na-NMF2 cell to 50% results on a more benign failure than the 100% SOC Li-FP cell. (E) summary of key parameters from each cell in the figure; Figure S3: Temperature (red, left y-axis) and voltage (black, right y-axis) responses to 1500 psi pneumatic nail penetration indicated by a green dashed line for a Li-NCA (A) and Li-FP (B) cells; Figure S4: Spectra of each acid gas HF (A), HCN (B), and HN_3 (C) at their peak detection compared to the standard they were fitted to in the quantification region. Each gas was analyzed in this way to confirm confidence in the software's gas detection; Figure S5: Na-NMF2 thermal ramp experiment replicate showing venting but no thermal runaway. (All experiments were completed at least twice to confirm the reported data was representative.); Figure S6: Thermal ramp of the Li-NCA cell charged to 100% SOC was carried out up to 180 °C to examine off gases. The cells were sealed in a pressure vessel purged with N_2 and connected with a heated line (180 °C) to an FTIR-g system. (A) The cell voltage (black), temperature (red), and chamber pressure in (blue) are shown over the experiment. (B) The concentration of CO, CO_2, CH_4, and carbonates are plotted over the duration of the thermal ramp on the left y-axis and with error in the measurement a shaded region above and below the corresponding line. The skin temperature is plotted in red on the right y-axis. lower concentrations of the same gases in (B) are plotted in (C). (D) The concentration of HF over the duration of the thermal ramp on the left y-axis again with the skin temperature on the right y-axis; Figure S7: Thermal ramp of the Li-FP cell charged to 100% SOC was carried out up to 180 °C to examine off gases. The cells were sealed in a pressure vessel purged with N_2 and connected with a heated line (180 °C) to an FTIR-g system. (A) The cell voltage (black), temperature (red), and chamber pressure in (blue) are shown over the experiment. (B) The concentration of CO, CO_2, CH_4, and carbonates are plotted over the duration of the thermal ramp on the left y-axis and with error in the measurement a shaded region above and below the corresponding line. The skin temperature is plotted in red on the right y-axis. (C) The concentration of HF over the duration of the thermal ramp on the left y-axis again with the skin temperature on the right y-axis.

Author Contributions: Methodology, R.C., G.H.W. and P.J.W.; Software, D.H.; Validation, R.C.; Formal analysis, R.C., G.H.W., C.J., D.H. and P.J.W.; Investigation, C.J. and P.J.W.; Resources, R.C., G.H.W. and C.T.L.; Data curation, R.C., G.H.W. and D.H.; Writing—original draft, R.C.; Writing—review & editing, G.H.W., C.J., D.H., P.J.W. and C.T.L.; Visualization, C.T.L.; Project administration, R.C.; Funding acquisition, R.C. All authors have read and agreed to the published version of the manuscript.

Funding: This research was funded by DOT PHMSA grant number O2412069017050353.

Data Availability Statement: The original contributions presented in this study are included in the article/Supplementary Material. Further inquiries can be directed to the corresponding author.

Acknowledgments: The authors acknowledge funding and technical support from DOT PHMSA.

Conflicts of Interest: Authors Connor Jacob and Dillon Hayman were employed by the company Precise Systems. The remaining authors declare that the research was conducted in the absence of any commercial or financial relationships that could be construed as a potential conflict of interest.

References

1. Whittingham, M.S. Chemistry of intercalation compounds: Metal guests in chalcogenide hosts. *Prog. Solid State Chem.* **1978**, *12*, 41–99. [CrossRef]
2. Doeff, M.M.; Ma, Y.; Visco, S.J.; De Jonghe, L.C. Electrochemical Insertion of Sodium into Carbon. *J. Electrochem. Soc.* **1993**, *140*, L169. [CrossRef]
3. Olivetti, E.A.; Ceder, G.; Gaustad, G.G.; Fu, X. Lithium-Ion Battery Supply Chain Considerations: Analysis of Potential Bottlenecks in Critical Metals. *Joule* **2017**, *1*, 229–243. [CrossRef]
4. Gao, Y.; Zhang, H.; Peng, J.; Li, L.; Xiao, Y.; Li, L.; Liu, Y.; Qiao, Y.; Chou, S.-L. A 30-year overview of sodium-ion batteries. *Carbon Energy* **2024**, *6*, e464. [CrossRef]
5. Hirsh, H.S.; Li, Y.; Tan, D.H.S.; Zhang, M.; Zhao, E.; Meng, Y.S. Sodium-Ion Batteries Paving the Way for Grid Energy Storage. *Adv. Energy Mater.* **2020**, *10*, 2001274. [CrossRef]
6. Hwang, J.-Y.; Myung, S.-T.; Sun, Y.-K. Sodium-ion batteries: Present and future. *Chem. Soc. Rev.* **2017**, *46*, 3529–3614. [CrossRef]
7. Li, M. Elevating the Practical Application of Sodium-Ion Batteries through Advanced Characterization Studies on Cathodes. *Energies* **2023**, *16*, 8004. [CrossRef]
8. Dubarry, M.; Beck, D. Communication—Forecast of the Impact of Degradation Modes on a Commercial Hard Carbon/Na3V2(PO4)2F3-based Na-ion Battery. *J. Electrochem. Soc.* **2024**, *171*, 080541. [CrossRef]
9. He, M.; Mejdoubi, A.E.L.; Chartouni, D.; Morcrette, M.; Troendle, P.; Castiglioni, R. High power NVPF/HC-based sodium-ion batteries. *J. Power Sources* **2023**, *588*, 233741. [CrossRef]
10. Li, M.; Du, Z.; Khaleel, M.A.; Belharouak, I. Materials and engineering endeavors towards practical sodium-ion batteries. *Energy Storage Mater.* **2020**, *25*, 520–536. [CrossRef]
11. Dorau, F.; Sommer, A.; Koloch, J.; Roess-Ohlenroth, R.; Schreiber, M.; Neuner, M.; Abo Gamra, K.; Lin, Y.; Schöberl, J.; Bilfinger, P.; et al. Comprehensive Analysis of Commercial Sodium-Ion Batteries: Structural and Electrochemical Insights. *J. Electrochem. Soc.* **2024**, *171*, 090521. [CrossRef]
12. Desai, P.; Huang, J.; Foix, D.; Tarascon, J.-M.; Mariyappan, S. Zero volt storage of Na-ion batteries: Performance dependence on cell chemistry! *J. Power Sources* **2022**, *551*, 232177. [CrossRef]
13. Chak, C.; Jayakumar, R.; Shipitsyn, V.; Bass, E.; McCloskey, R.; Zuo, W.; Le, P.M.L.; Xu, J.; Ma, L. Unveiling the Thermal Stability of Sodium Ion Pouch Cells Using Accelerating Rate Calorimetry. *J. Electrochem. Soc.* **2024**, *171*, 070512. [CrossRef]
14. Xie, Y.; Xu, G.-L.; Che, H.; Wang, H.; Yang, K.; Yang, X.; Guo, F.; Ren, Y.; Chen, Z.; Amine, K.; et al. Probing Thermal and Chemical Stability of NaxNi1/3Fe1/3Mn1/3O2 Cathode Material toward Safe Sodium-Ion Batteries. *Chem. Mater.* **2018**, *30*, 4909–4918. [CrossRef]
15. Chen, J.; Rui, X.; Hsu, H.; Lu, L.; Zhang, C.; Ren, D.; Wang, L.; He, X.; Feng, X.; Ouyang, M. Thermal runaway modeling of LiNi0.6Mn0.2Co0.2O2/graphite batteries under different states of charge. *J. Energy Storage* **2022**, *49*, 104090. [CrossRef]
16. Frith, J.T.; Lacey, M.J.; Ulissi, U. A non-academic perspective on the future of lithium-based batteries. *Nat. Commun.* **2023**, *14*, 420. [CrossRef]
17. Chen, S.; Niu, C.; Lee, H.; Li, Q.; Yu, L.; Xu, W.; Zhang, J.-G.; Dufek, E.J.; Whittingham, M.S.; Meng, S.; et al. Critical Parameters for Evaluating Coin Cells and Pouch Cells of Rechargeable Li-Metal Batteries. *Joule* **2019**, *3*, 1094–1105. [CrossRef]
18. Klein, E.J.; Carter, R.; Love, C.T.; Klein, E.J.; Love, C.T. Accelerating Rate Calorimetry and Complementary Techniques to Characterize Battery Safety Hazards. *JoVE* **2021**, *175*, e60342. [CrossRef]
19. Lei, B.; Zhao, W.; Ziebert, C.; Uhlmann, N.; Rohde, M.; Seifert, H.J. Experimental Analysis of Thermal Runaway in 18650 Cylindrical Li-Ion Cells Using an Accelerating Rate Calorimeter. *Batteries* **2017**, *3*, 14. [CrossRef]
20. Nguyen, T.P.; Kim, I.T. Recent Advances in Sodium-Ion Batteries: Cathode Materials. *Materials* **2023**, *16*, 6869. [CrossRef]
21. Hu, J.; Xu, L.; Li, X.; Liang, Q.; Ding, C.; Li, Y.; Liu, Y.; Gao, Y. Pre-sodiation strategies for constructing high-performance sodium-ion batteries. *J. Mater. Chem. A* **2025**. [CrossRef]
22. Gupta, P.; Pushpakanth, S.; Haider, M.A.; Basu, S. Understanding the Design of Cathode Materials for Na-Ion Batteries. *ACS Omega* **2022**, *7*, 5605–5614. [CrossRef] [PubMed]
23. Tarascon, J.-M. Na-ion versus Li-ion Batteries: Complementarity Rather than Competitiveness. *Joule* **2020**, *4*, 1616–1620. [CrossRef]
24. Yang, C.; Xin, S.; Mai, L.; You, Y. Materials Design for High-Safety Sodium-Ion Battery. *Adv. Energy Mater.* **2021**, *11*, 2000974. [CrossRef]
25. Laufen, H.; Klick, S.; Ditler, H.; Quade, K.L.; Mikitisin, A.; Blömeke, A.; Schütte, M.; Wasylowski, D.; Sonnet, M.; Henrich, L.; et al. Multi-method characterization of a commercial 1.2 Ah sodium-ion battery cell indicates drop-in potential. *Cell Rep. Phys. Sci.* **2024**, *5*, 101945. [CrossRef]
26. Li, Y.; Hu, Y.-S.; Qi, X.; Rong, X.; Li, H.; Huang, X.; Chen, L. Advanced sodium-ion batteries using superior low cost pyrolyzed anthracite anode: Towards practical applications. *Energy Storage Mater.* **2016**, *5*, 191–197. [CrossRef]

27. Robinson, J.B.; Finegan, D.P.; Heenan, T.M.M.; Smith, K.; Kendrick, E.; Brett, D.J.L.; Shearing, P.R. Microstructural Analysis of the Effects of Thermal Runaway on Li-Ion and Na-Ion Battery Electrodes. *J. Electrochem. Energy Convers. Storage* **2017**, *15*, 011010. [CrossRef]
28. Yue, Y.; Jia, Z.; Li, Y.; Wen, Y.; Lei, Q.; Duan, Q.; Sun, J.; Wang, Q. Thermal runaway hazards comparison between sodium-ion and lithium-ion batteries using accelerating rate calorimetry. *Process Saf. Environ. Prot.* **2024**, *189*, 61–70. [CrossRef]
29. Zhou, Q.; Li, Y.; Tang, F.; Li, K.; Rong, X.; Lu, Y.; Chen, L.; Hu, Y.-S. Thermal Stability of High Power 26650-Type Cylindrical Na-Ion Batteries. *Chin. Phys. Lett.* **2021**, *38*, 076501. [CrossRef]
30. Bischof, K.; Marangon, V.; Kasper, M.; Aracil Regalado, A.; Wohlfahrt-Mehrens, M.; Hölzle, M.; Bresser, D.; Waldmann, T. Evaluation of commercial 18650 and 26700 sodium-ion cells and comparison with well-established lithium-ion cells. *J. Power Sources Adv.* **2024**, *27*, 100148. [CrossRef]
31. He, M.; Davis, R.; Chartouni, D.; Johnson, M.; Abplanalp, M.; Troendle, P.; Suetterlin, R.-P. Assessment of the first commercial Prussian blue based sodium-ion battery. *J. Power Sources* **2022**, *548*, 232036. [CrossRef]
32. Bugryniec, P.J.; Resendiz, E.G.; Nwophoke, S.M.; Khanna, S.; James, C.; Brown, S.F. Review of gas emissions from lithium-ion battery thermal runaway failure—Considering toxic and flammable compounds. *J. Energy Storage* **2024**, *87*, 111288. [CrossRef]
33. Larsson, F.; Andersson, P.; Blomqvist, P.; Mellander, B.-E. Toxic fluoride gas emissions from lithium-ion battery fires. *Sci. Rep.* **2017**, *7*, 10018. [CrossRef] [PubMed]
34. Rappsilber, T.; Yusfi, N.; Krüger, S.; Hahn, S.-K.; Fellinger, T.-P.; Krug von Nidda, J.; Tschirschwitz, R. Meta-analysis of heat release and smoke gas emission during thermal runaway of lithium-ion batteries. *J. Energy Storage* **2023**, *60*, 106579. [CrossRef]
35. Drake, S.J.; Martin, M.; Wetz, D.A.; Ostanek, J.K.; Miller, S.P.; Heinzel, J.M.; Jain, A. Heat generation rate measurement in a Li-ion cell at large C-rates through temperature and heat flux measurements. *J. Power Sources* **2015**, *285*, 266–273. [CrossRef]
36. Carter, R.; Huhman, B.; Love, C.T.; Zenyuk, I.V. X-ray computed tomography comparison of individual and parallel assembled commercial lithium iron phosphate batteries at end of life after high rate cycling. *J. Power Sources* **2018**, *381*, 46–55. [CrossRef]
37. Fear, C.; Juarez-Robles, D.; Jeevarajan, J.A.; Mukherjee, P.P. Elucidating Copper Dissolution Phenomenon in Li-Ion Cells under Overdischarge Extremes. *J. Electrochem. Soc.* **2018**, *165*, A1639. [CrossRef]
38. He, Y.; Shang, W.; Tan, P. Insight into rechargeable batteries in extreme environment for deep space exploration. *Carbon Neutralization* **2024**, *3*, 773–780. [CrossRef]

Disclaimer/Publisher's Note: The statements, opinions and data contained in all publications are solely those of the individual author(s) and contributor(s) and not of MDPI and/or the editor(s). MDPI and/or the editor(s) disclaim responsibility for any injury to people or property resulting from any ideas, methods, instructions or products referred to in the content.

TECHNICAL REPORT DOCUMENTATION PAGE

1. Report No.	2. Government Accession No.	3. Recipient's Catalog No.
4. Title and Subtitle First Look at Safety and Performance Evaluation of Commercial Sodium-Ion Batteries		5. Report Date January 31, 2025
		6. Performing Organization Code:
7. Author(s) Rachel Carter, Gordon Waller, Connor Jacob, Dillon Hayman, Patrick J. West, Corey T. Love		8. Performing Organization Report No.
9. Performing Organization Name and Address US Naval Research Laboratory 4555 Overlook Ave SW Washington, DC 20375		10. Work Unit No. 61-1W45-0-1-5
		11. Contract or Grant No. 693JK323N00010
12. Sponsoring Agency Name and Address US DOT – Pipeline and Hazardous Materials Safety Administration Office of Hazardous Materials Safety 1200 New Jersey Ave SE Washington, DC 20590		13. Type of Report and Period
		14. Sponsoring Agency Code PHH-63

15. Supplementary Notes

16. Abstract

Herein, we investigate the performance and safety of four of the early-stage, commercial Na-ion batteries available in 2024, representing the most popular cathode types across research and commercialization: polyanion (Na-VPF), layered metal oxide (Na-NMF), and a Prussian blue analog (Na-tmCN). The cells deliver a wide range of energy density with Na-tmCN delivering the least (23 Wh/kg) and Na-NMF delivering the most (127 Wh/kg). The Na-VPF cell was in between (47 Wg/kg). Capacity retention under specified cycling conditions and with periodic 0 V excursions was the most robust for the Na-tmCN cells in both cases. Accelerating rate calorimetry (ARC) and nail penetration testing finds that Na-NMF cells do undergo thermal runaway in response to abuse, while the Na-VPF and Na-tmCN exhibit only low self-heating rates (<1 ◦C/min). During these safety tests, all cells exhibited off-gassing, so we conducted in-line FTIR equipped with a heated gas cell to detect CO, CO2, CH4, toxic acid gases (HCN, HF, NH3), and typical electrolyte components (carbonate ester solvents). Gases similar to those detected during Li-ion failures were found in addition to HCN for the Na-tmCN cell. Our work compares different types of commercial Na-ion batteries for the first time, allowing for a more holistic comparison of the safety and performance tradeoffs for different Na-ion cathode types emerging in 2024.

17. Key Words	18. Distribution Statement
sodium-ion battery; accelerated rate calorimetry; safety testing; commercial cells	No restrictions

19. Security Classif. (of this report)	20. Security Classif. (of this page)	21. No. of Pages	22. Price
Unclassified	Unclassified	16	

Form DOT F 1700.7 (8-72) Reproduction of completed page authorized